Non-contrast MR imaging of blood-brain barrier permeability to water

Lin, Z.X.; Li, Y.; Su, P.; Mao, D.; Wei, Z.L.; Pillai, J.J.; … ; Lu, H.Z.

Non-contrast MR imaging of blood-brain-barrier permeability to water

Zixuan Lin[1], Yang Li[2,3], Pan Su[2,3], Deng Mao[2,3], Zhiliang Wei[2,4], Jay J. Pillai[2,5], Abhay Moghekar[6], Matthias van Osch[7], Yulin Ge[8], and Hanzhang Lu[1,2,4]

[1]Department of Biomedical Engineering, Johns Hopkins University School of Medicine, Baltimore, Maryland, USA.
[2]The Russell H. Morgan Department of Radiology & Radiological Science, Johns Hopkins University School of Medicine, Baltimore, Maryland, USA.
[3]Graduate School of Biomedical Sciences, University of Texas Southwestern Medical Center, Dallas, Texas, USA.
[4]F. M. Kirby Research Center for Functional Brain Imaging, Kennedy Krieger Research Institute, Baltimore, Maryland, USA.
[5]Department of Neurosurgery, Johns Hopkins University School of Medicine, Baltimore, Maryland, USA
[6]Department of Neurology, Johns Hopkins University School of Medicine, Baltimore, Maryland, USA.
[7]Department of Radiology, C. J. Gorter Center for High Field MRI, Leiden University Medical Center, Leiden, Netherlands
[8]Department of Radiology, New York University Langone Medical Center, New York, New York, USA.

Corresponding author:
Hanzhang Lu, Ph.D.
The Russell H. Morgan Department of Radiology and Radiological Science
Johns Hopkins University School of Medicine
600 N. Wolfe Street, Park 322
Baltimore, MD 21287
Email: hanzhang.lu@jhu.edu
Phone: 410-955-1431
Fax: 410-614-1977

Word Count: 5000
Running Title: Non-contrast measurement of BBB permeability

ABSTRACT

Purpose: Many brain diseases are associated with an alteration in blood-brain-barrier (BBB) and its permeability. Current methods using contrast-agent are primarily sensitive to major leakage of BBB to macromolecules, but may not detect subtle changes in BBB permeability. The present study aims to develop a novel non-contrast MRI technique for the assessment of BBB permeability to water.

Methods: The central principle is that by measuring arterially labeled blood spins that are drained into cerebral veins, water extraction fraction (E) and permeability-surface-area product (PS) of BBB can be determined. Four studies were performed. We first demonstrated the proof-of-principle using conventional ASL with very long post-labeling delays (PLD). Next, a new sequence, dubbed water-extraction-with-phase-contrast-arterial-spin-tagging (WEPCAST), and its Look-Locker (LL) version were developed. Finally, we demonstrated that the sensitivity of the technique can be significantly enhanced by acquiring the data under mild hypercapnia.

Results: By combining a strong background suppression with long PLDs (2500ms–4500ms), ASL spins were reliably detected in the superior sagittal sinus (SSS), demonstrating the feasibility of measuring this signal. The WEPCAST sequence eliminated partial voluming effects of tissue perfusion and allowed quantitative estimation of E =95.5±1.1% and PS =188.9±13.4mL/100g/min, which were in good agreement with literature reports. LL-WEPCAST sequence shortened the scan time from 19min to 5min while providing results consistent with multiple single-PLD acquisitions. Mild hypercapnia increased SNR by 78±25% without causing a discomfort in participants.

Conclusion: A new non-contrast technique for the assessment of global BBB permeability was developed, which may have important clinical applications.

INTRODUCTION

Blood-brain barrier (BBB) is one of the most important central nervous system (CNS) barriers. By regulating the blood-brain exchange of substances, BBB functions to restrict macromolecules and neurotoxins, which provides a constant microenvironment that is crucial for the normal function of nervous system (1). Disruption of BBB has been associated with many pathological conditions, such as Alzheimer's disease (2), multiple sclerosis (3), amyotrophic lateral sclerosis (4), brain tumor (5), stroke (6), Parkinson's disease (7), etc. The ability to transiently maneuver the BBB permeability has also been exploited for efficient drug delivery in diseases like brain tumor, lysosomal storage disease and Parkinson's disease (8-10). Therefore, a technique to report the permeability of BBB in humans will have a tremendous potential in clinical applications.

At present, the most widely used method to evaluate BBB permeability is by using Gadolinium (Gd) contrast agent and observing post-contrast T_1 enhancement qualitatively or measuring and modeling dynamic contrast-enhanced (DCE) MRI signal quantitatively (11). While this method is elegantly sensitive to major breakdowns of BBB (to the extent that large molecules like gadolinium diethylenetriamine pentaacetic acid, Gd-DTPA with a molecular weight of 547g/mol, become permeable), its ability to detect small disruption of BBB at early stage of a disease is more challenging (12-14). Furthermore, contrast-enhanced MRI is still not a common procedure in many diseases such as Alzheimer's disease, traumatic brain injury, and virtually all psychiatric disorders, due to concerns related to the injection of exogenous agent, potential side effects of nephrogenic systemic fibrosis (NSF), deposition of Gd molecules, and potential neurotoxicity (15,16). Therefore, a non-contrast method to assess BBB permeability is expected to open an array of new research avenues and could translate to clinical screening and management of many brain diseases.

The central goal of our study is to measure BBB permeability to water without using any exogenous contrast agent, based on the following considerations. Water is a small molecule (18g/mol) and it may be more sensitive to early changes of BBB in diseases (17). Water is the main source of MRI signal and thus may provide sufficient sensitivity without the assistance of exogenous agent. Manipulation and modeling of the water signal in the blood have provided useful information related to perfusion and other hemodynamic parameters, as shown by extensive work in the Arterial Spin Labeling (ASL) field (18-24).

3

In a healthy brain, water has high but not 100% permeability across BBB. Previous work using invasive methods has suggested that 90-95% of the water molecules in the arterial blood cross the BBB and enter brain tissues in a single pass (25-28). This water extraction fraction, E, together with cerebral blood flow (CBF) can be used to quantify the permeability index, referred to as permeability-surface-area product (PS). Since many imaging techniques exist to measure CBF, the main technical challenge therefore lies in the determination of water extraction fraction in perfusing blood.

In this work, we conducted a series of four studies to develop a technique to quantify global water extraction fraction and PS based on the general principle of ASL. Our central hypothesis is that arterially labeled blood spins can be divided into those that enter the tissue (i.e. being extracted by BBB) and those that pass through the microvasculature to enter the venous vessels, and that their relative fraction can be determined. We first used a background-suppressed ASL sequence with a very long post-labeling delay (PLD) of up to 4500ms to demonstrate that ASL signal in the venous vessels, e.g. in superior sagittal sinus (SSS), can be reliably measured. We next developed a new sequence, water extraction with phase contrast arterial spin tagging (WEPCAST), to selectively detect venous ASL signals without the confounding contributions of tissue perfusion spins. In the third study, we employed Look-Locker acquisition in WEPCAST while ensuring signal suppression of static tissue and blood signal at each PLD, which allowed significant reduction in scan time. Finally, we demonstrated that hypercapnia can drastically enhance the sensitivity of the technique, and that hyperoxic-hypercapnia did not provide further benefits.

METHODS

Theory

According to the Renkin-Crone Model (29,30), BBB permeability can be represented by permeability-surface-area product (PS) per unit mass of tissue, which can be calculated as

$$PS = -\ln(1 - E) \cdot f \qquad [1]$$

where E is the extraction fraction of the water and f is CBF. Considerable work in the literature has studied techniques of CBF measurement (24,31-34). Thus the bulk of this work will concentrate on the measurement of E.

With pseudo-continuous ASL (pCASL), we can label the water molecules in the incoming arterial blood. These labeled spins then travel through arterial trees to reach the capillary-tissue interface. Under the limited diffusion regime, the extraction of labeled spins at the capillary-tissue interface can be illustrated by Figure 1a. The majority of the labeled spins are extracted to tissue (Figure 1a red arrow), whereas the non-extracted spins are drained directly to the venous system (blue arrow). Additionally, a small amount of labeled spins that are extracted to tissue will re-exchange back into the vascular system (yellow arrow). Specifically, for SSS where our experimental measurement is performed, the blood spins consist of following three components: (a) non-extracted arterial spins; (b) extracted arterial spins that were re-exchanged into vessel; and (c) non-labeled spins that came to vessel from tissue through exchange. For each component, their control, label, and difference signals can be derived (see Supporting Methods). As far as the difference signal is concerned, only spins from part (a) and part (b) are non-zero, as part (c) signal is canceled out during the control and label subtraction (see Supporting Methods).

Without considering temporal signal smoothing due to bolus dispersion or regional variations in arrival time, the ASL difference signal from part (a) can be written as (see Supporting Methods):

$$\Delta M_{a,unsm}(t) = 2\alpha(1-E)M_0 e^{-\frac{\delta_v}{T_{1,blood}}} c(t), \tag{2}$$

where M_0 is the equilibrium magnetization of blood (MR signal/100 mL blood), $T_{1,blood}$ is blood T_1, δ_v is bolus arrival time (BAT) of spins to SSS, α is labeling efficiency, $c(t) = \begin{cases} 1, & if\,\delta_v < t < \delta_v + \tau \\ 0, & otherwise \end{cases}$ is arterial input function, and τ is labeling duration. Note that, in this signal component, the inverted spins always relax at the T_1 of blood. Thus, tissue T_1 is not present in the equation. Typical signal curve is illustrated in Figure 1b (blue). Next, to account for dispersion of the labeled bolus as well as the smoothing effect in an ROI analysis (i.e. different voxels in the ROI may have different δ_v), Eq. [2] was convolved with a Gaussian kernel with variance σ^2, resulting in a smoothed signal as follows:

$$\Delta M_{a,sm}(t) = 2\alpha(1-E)M_0 e^{-\frac{\delta_v}{T_{1,blood}}} c(t) \otimes G(t), \tag{3}$$

in which $G(t) = \frac{1}{\sqrt{2\pi\sigma^2}} e^{-t^2/2\sigma^2}$ denotes the Gaussian kernel and $\otimes$ denotes convolution operation. Figure 1c (blue) illustrates the smoothed signal as a function of time.

For contributions from part (b), the ASL difference signal without bolus dispersion can be written as (see Supporting Methods for derivation details):

$$\Delta M_{b,unsm}(t) = 2\alpha f/\lambda E M_0 e^{-\frac{\delta_v}{T_{1,blood}}} c(t) \otimes [r(t)m(t)],$$ [4]

where $r(t) = e^{-ft/\lambda}$ is residue function of labeled spins in tissue, λ is blood-brain partition coefficient of water, $m(t) = e^{-t/T_{1,tissue}}$ represents T_1 relaxation in tissue ($T_{1,tissue}$). Note that the longitudinal relaxation process of these inverted spins includes both relaxation while they are in blood vessels (relaxing at T_1 of blood, denoted by the exponential term in Eq. [4]) and relaxation while they are in tissue (relaxing at T_1 of tissue, denoted by the convolution term as the time they spend in tissue varies). Figure 1b (yellow) illustrates a typical signal curve. Then, we added the dispersion effects by convolving Eq. [4] with a Gaussian kernel, resulting in a smoothed signal:

$$\Delta M_{b,sm}(t) = 2\alpha f/\lambda E M_0 e^{-\frac{\delta_v}{T_{1,blood}}} c(t) \otimes [r(t)m(t)] \otimes G(t),$$ [5]

Therefore, the total SSS ASL signal equals to

$$\Delta M_{ASL,sm}(t) = \Delta M_{a,sm}(t) + \Delta M_{b,sm}(t).$$ [6]

To provide an illustration of the expected signal, Figure 1c displays results of numerical simulations of each signal component as well as their sum. It can be seen that, after the bolus arrives at the SSS (around 4s after labeling), the signal starts to rise. The signal from non-extracted spins (blue curve) rises more rapidly and lasts for a period corresponding to the labeling duration. In contrast, the signal from spins that were re-exchanged out of tissue (yellow curve) rises slower and lasts longer. It is also important to point out that the vast majority of the signal is originated from the non-extracted spins (i.e. component a) while the re-exchanged spins (i.e. component b) only contribute to a small fraction.

Once experiments are performed to measure $\Delta M_{ASL,sm}$ as a function of time, i.e. PLD, model fitting can be performed using the above-described theoretical framework. In the fitting, $\Delta M_{ASL,sm}$ and M_0 are experimental measures. E, δ_v and FWHM of the Gaussian dispersion kernel (σ) are unknown model parameters to be estimated from the fitting. The other parameters are known model parameters based on the literature: $T_{1,blood}$=1841ms (35), $T_{1,tissue}$=1165ms (23), α=0.86 (36) and $\lambda = 0.9$mL/g (31). We have also conducted testings to examine to what extent the estimated E was dependent on the assumed values by varying the assumed values by +/-10% for each variable.

MRI Experiments

The experiments were performed on a 3T (Philips) system. The study was approved by the Johns Hopkins University Institutional Review Board and informed written consent was obtained from all subjects before participation. A total of 23 participants (age: 26±6 years, male/female: 11/12) were enrolled in this study.

Study I – Proof-of-principle with background-suppressed, long PLD pCASL sequence

We started the project by demonstrating that labeled ASL signal in the venous vessel, albeit small, can be robustly detected by using a long PLD in combination with sufficient suppression of background tissue, blood and CSF signals. Six healthy subjects were enrolled (age: 27±6 years, male/female: 3/3). Figure 2a illustrates the pCASL sequence used in this study. Background suppression was achieved by applying a spatially selective pre-saturation pulse (1500ms before labeling) followed by five inversion pulses: one selective pulse before labeling module and four non-selective inversion pulses during the PLD (37). The pulse timing was optimized to suppress background signal for a range of T_1-values (750ms–4800ms) to <5% of equilibrium magnetization. The labeling duration was set to 2000ms. Considering the expected BAT at SSS, six long PLDs, acquired in separate scans, were used: PLD=2000, 2500, 3000, 3500, 4000, 4500ms. Other imaging parameters were: single slice mid-sagittal plane for the imaging slice, voxel size=3.13×3.13mm, slice thickness=10mm, TE=9.5ms, 30 pairs. We fixed the recovery time (from RF excitation to the pre-sat of next TR) for different scans (116ms), thus TR varied with PLD: 5643, 6143, 6643, 7143, 7643, 8143ms. The scan duration varied from 5.6 to 7.1min. An additional $M_{0,ASL}$ scan with same TE and a long TR=10s was acquired for quantification purposes.

Study II – Selective imaging of venous ASL signal by water-extraction-with-phase-contrast-arterial-spin-tagging (WEPCAST) MRI

To improve the efficiency of measuring venous ASL signal and reduce the confounding contribution of tissue perfusion signal, we devised a new sequence, dubbed as WEPCAST MRI, by adding a phase-contrast velocity-encoding gradient during imaging acquisition of the pCASL sequence. Figure 2b displays these additions in the sequence diagram. Note that the purpose of

this bipolar gradient is different from the commonly used crusher gradient in that it uses complex subtraction to isolate pure blood signal, rather than dephasing blood signal. The velocity-encoding gradient modifies the venous ASL signal written in Eq. [6] to be:

$$\Delta M_{WEPCAST,sm}(t) = 2\Delta M_{ASL,sm}(t)\left|sin\left(\frac{\pi v}{2V_{enc}}\right)\right| \qquad [7]$$

where v is the velocity of blood, V_{enc} is the encoding velocity such that $\gamma m_1 V_{enc} = \pi/2$, and m_1 is the first moment of the gradient waveform (38). Thus, four types of images are necessary for a complete dataset: a pair of images are acquired with label and control pulses, respectively, and each is acquired twice with opposite bipolar gradients following the RF excitation. Note that the use of the phase-contrast scheme results in the measured difference signal being dependent on a new variable, v. To mitigate the need of adding v to the fitting parameter set, we also applied the same phase-contrast scheme with identical V_{enc} when acquiring the M_0 image. That is, the acquired M_0 in WEPCAST MRI is:

$$M_{0,WEPCAST} = 2M_{0,ASL}\left|sin\left(\frac{\pi v}{2V_{enc}}\right)\right| \qquad [8]$$

Therefore, the model fitting procedure for WEPCAST MRI is identical to that for the conventional pCASL described in the Theory section.

Six healthy subjects were examined (age: 23±3 years, male/female: 3/3). The imaging protocol was the same as that in study I except for the following: V_{enc}=15cm/s, PLDs=3000, 3500, 4000, 4500ms, TE=13ms, 15 pairs, scan duration 6.7, 7.2, 7.7, and 8.2min, respectively. The V_{enc} chosen was based on typical peak velocity in SSS (38,39). An additional $M_{0,WEPCAST}$ image, i.e. a scan with same bipolar gradient but with a long TR=10s, was acquired for quantification.

Study III – Expediting data acquisition by using a background-suppressed Look-Locker WEPCAST sequence

Acquisition of multi-PLD data in separate scans is useful for proof-of-principle, but is time-consuming for clinical applications. The purpose of this study was therefore to expedite the acquisition by applying a Look-Locker readout. Figure 2c depicts the schematic diagram of the sequence. After the labeling duration, eight images were acquired sequentially at PLD=1500, 2000, 2500, 3000, 3500, 4000, 4500, 5000ms. Background suppression was also applied for all PLDs. Two types of background suppression schemes were considered. One, referred to as tissue

suppression, was the attenuation of tissue signal in the imaging slice. These suppression pulses (blue blocks in Figure 2c) consist of two non-selective inversion pulses between consecutive acquisitions. Together with the effect of excitation pulses (gray blocks), the static tissue signal in the imaging slice can be maintained to be <5% of the equilibrium magnetization for every PLD. However, these pulses do not suppress the blood signal outside the imaging slice, as those spins do not experience the excitation pulses. Venous blood spins outside the imaging slice come from two sources: those originally in the brain tissue and those originally in the arterial blood. While those from the arterial blood are our targeted signal, the spins originated from the tissue need to be suppressed. Suppression of these signals turned out to be critical for the quality of the data. Although the subtraction between the control and label scans should ideally cancel out these signals, in practice pulsation of flow will result in imperfect cancellation thus manifesting as physiological noise in the data. Thus, a second series of background suppression pulses, referred to as vessel suppression, were needed (red blocks in Figure 2c), which consist of two non-selective inversion pulses between the end of labeling module and first acquisition. The timing was optimized to suppress the control blood signal in SSS to be <5% of equilibrium magnetization over a range of blood T_1 and tissue T_1, but not affecting difference signal.

In one cohort of six healthy subjects (age: 29±7 years, male/female: 3/3), we examined the benefit of the background suppression schemes. The imaging slice was planned coronally and the location was chosen to be at the posterior SSS. Other imaging parameters were as follows: labeling duration=2000ms, V_{enc} =15cm/s, voxel size=3.13×3.13mm, slice thickness=10mm, TR=7546ms, TE=9.2ms, 10 pairs, scan duration=5min3s. Note that, in contrast to other Look-Locker ASL sequences (which usually use a flip angle between 20-40°) (40-43), the flip angle used here was 90°. This allows the signal to be maximized and takes advantage of the fact that fresh inflow blood will replace the saturated blood for each PLD. Four different sequences were performed to evaluate the effect of background suppression: one with both vessel and tissue suppression pulses, one with only vessel suppression pulses, one with only tissue suppression pulses, one with no suppression pulses. Additionally, an $M_{0,WEPCAST}$ image was acquired using a TR of 10s.

In another cohort of six healthy subjects (age: 28±8 years, male/female: 3/3), we conducted a comparison between the Look-Locker and multiple single-PLD WEPCAST sequence. Each subject received both the protocols described in study II (19min47s) and III

(5min3s). $M_{0,WEPCAST}$ images were also collected for the single-PLD and Look-Locker data sets, respectively.

Study IV – Enhancing sensitivity by CO_2 inhalation

Hypercapnia challenge via CO_2 inhalation is known to increase CBF. It can be seen from Eq. [1] that, when CBF increases, E will decrease and more labeled spins will be measured in the vein. Furthermore, the measured signal will also increase due to several other factors: 1) CO_2 reduces BAT (δ_v); 2) CO_2 increases T_2^* of blood, thus M_0. Collectively, we anticipate that CO_2 inhalation will augment the WEPCAST signal. Note that although hypercapnia is expected to reduce E, previous literature has suggested that PS will remain relatively constant under mild hypercapnia, and therefore this physiological parameter of interest (i.e. PS) can still be measured, despite the 'experimental' modulation of E and CBF to enhance the SNR. Modulation of inspired air content was achieved using a breathing apparatus described in Lu et al (44). The CO_2 gas mixture contains the following contents: 2.5% CO_2, 21% O_2 and 76.5% N_2. Note that this is a very mild hypercapnia challenge, as most studies in the literature use 5% CO_2 (45,46). Additionally, we also tested the benefit of hyperoxia challenge (on top of hypercapnia), as an increase in venous oxygenation may further enhance the signal intensity (via an increase in T_2^*). The hyperoxic-hypercapnia challenge used the following gas mixture: 2.5% CO_2, 58% O_2 and 39.5% N_2.

Five healthy subjects were enrolled (age: 28±5 years, male/female: 2/3). Each participant received a normocapnia (breathing room-air), hypercapnia (breathing CO_2 enriched gas), and hyperoxic-hypercapnia (breathing CO_2 and O_2 enriched gas) session in a sequential order. During each breathing state, the following sequences were performed: background-suppressed Look-Locker WEPCAST sequence and M_0 sequence as in study III for E measurement, and Phase-Contrast (PC) flow velocity MRI as in Peng et al (34) for global CBF measurement. During the entire experiment, end-tidal CO_2 was monitored and recorded using capnograph.

Data Analysis

The data were analyzed using in-house MATLAB (Mathworks, Natick, MA) scripts. For Study I which was based on a conventional pCASL sequence, pairwise subtraction was performed for control and label images to obtain difference images. Three regions-of-interest

(ROIs) were drawn manually corresponding to anterior, middle, and posterior segments of the SSS, which allowed us to compare the temporal dynamics of the labeled spins along the SSS. Averaged signals in each ROI were calculated for each PLD. The signals were corrected for imperfections of the background suppression pulse, with an assumption of an inversion efficiency=0.98 for each inversion pulse (47).

For Study II to IV which were based on the WEPCAST sequence, four types (i.e. two ASL types multiplied by two phase-contrast types) of raw images were obtained: control image with positive-bipolar, control image with negative-bipolar, label image with positive-bipolar, and label image with negative-bipolar. The positive-bipolar and negative-bipolar images were first combined using complex subtraction to obtain phase-contrast velocity-encoded control and label images. Then a subtraction between phase-contrast velocity-encoded control and label images results in the final difference images for all PLDs. An ROI was drawn encompassing the posterior SSS region. The ROI signal curve was fitted to the model using procedure described in the Theory section with Matlab function nlinfit.m, from which the water extraction fraction, E, was estimated. For Study II and III, the total CBF value was assumed as 55mL/100g/min for male and 62mL/100g/min for female subjects (34). Then PS value was calculated using Eq. [1].

For Study IV, E was estimated separately for each of the breathing conditions. The PC flow velocity MRI images were processed following methods described in Peng et al (34) to obtain total blood flow to the brain, which was normalized by brain volume (obtained with a T_1-weighted MPRAGE scan, TR/TE=8.1/3.7ms, 160 slices with an isotropic resolution of 1mm) to obtain unit mass CBF (in mL/100g/min). Then the PS values were obtained using Eq. [1].

RESULTS

Study I – Proof-of-principle with background-suppressed, long PLD pCASL sequence

Representative sagittal ASL difference images at different PLDs are shown in Figure 3a. A PLD of 2000ms is the typical value used in ASL studies and the image primarily reflects perfusion signal in the tissue. As the PLD increases (Figure 3a), the perfusion signal decays due to T_1 relaxation and overall image intensity becomes lower. In contrast, signal in major draining veins, e.g. SSS, becomes increasingly apparent in these long PLDs (arrows in Figure 3a). This is because SSS has an extended bolus arrival time and the labeled spins reach this location only at these long PLD values. Visual inspection of the signal in the SSS suggested that the ASL signal

first appears at anterior SSS, at about PLD=2500ms. Soon after that, the entire SSS becomes bright as the 2-second labeling bolus occupies the whole length of the SSS. Afterwards, the bolus drains away from this vessel and the signal diminishes in an anterior-to-posterior fashion, consistent with its known anatomy. A corresponding M_0 image is shown in Figure 3b. Quantitative ROI results of the signals at three segments of SSS (i.e. anterior, middle and posterior, see Figure 3c for examples) are shown in Figure 3d. It can be seen that the signal curve shifts to the right as the ROI moves posteriorly, reflecting an increase of BAT.

Study II – Selective imaging of venous ASL signal by WEPCAST MRI

Representative control, label, and difference images of WEPCAST MRI at a PLD=4000 ms are shown in Figure 4a. For comparison, images using the conventional sequence (i.e. that used in Study I) are also shown. Compared with conventional sequence, tissue signal in WEPCAST MRI is well suppressed, leaving only signal from venous vessels. Figure 4b displays WEPCAST difference images for all PLD values acquired. Also shown in Figure 4b is the M_0 image. The advantage of this M_0 image is that partial voluming effect from the tissue is minimized, which is important for accurate estimation of E and PS parameters. Quantitative analysis focused on the posterior portion of the SSS, which drains the majority of blood in the cerebral cortex and provides an assessment of global BBB permeability. Figure 4c shows a group-averaged signal curve (N=6). Model fitting of an individual data set is shown in Supporting Figure S1. Across all participants (N=6), the average E in young, healthy subjects was 95.5±1.1% and the PS was 188.9±13.4mL/100g/min. The dependence of the results on model assumptions is shown in Table 1, illustrating that the estimated E and PS did not change much when varying assumed parameters.

Study III – Expediting data acquisition by using a background-suppressed LL-WEPCAST sequence

LL-WEPCAST allows acquisition of multiple-PLD data in the time of a single scan. The imaging slice was placed coronally to allow fresh spins to replace saturated spins after every excitation. Difference images using various background-suppression schemes are illustrated in Figure 5. Group-averaged control signals in SSS (N=6) are shown in Figure 6a. Without the application of any background-suppression pulses (denoted as "None" in the figure), the control

signal of LL-WEPCAST is close to the equilibrium magnetization (yellow curve in Figure 6a), thus it is very difficult to detect a difference signal on the order of 0.5% (Figure 5). With the addition of tissue-suppression pulses, the tissue signal is well suppressed (data not shown) but the control signal in the SSS is still relatively large (gray curve in Figure 6a), because the inflowing blood was not suppressed. Thus, the difference images still contain considerable fluctuations, especially in the first few PLDs (Figure 5). With the additional application of vessel suppression pulses, the control signal in LL-WEPCAST is consistently suppressed to be less than 5% of M_0 (blue curve in Figure 6a). Accordingly, the intended venous ASL signal is more apparent in the difference image (Figure 5).

Figure 6b shows the difference signal curve using LL-WEPCAST with both tissue and vessel suppressions. Temporal SNR was found to be 1.36±0.70 (mean±SD, N=6) for each repetition within the PLD range of 3000-4000ms. The average E calculated for six subjects was 96.1±1.2% and the average PS value was 203.3±17.5mL/100g/min. The other three sequences were not able to give stable signals or converging fitting results.

In a separate cohort (N=6), we compared the LL with multiple single-PLD WEPCAST sequences. Averaged SSS signal curves acquired with these two sequences are shown in Figure 7a. Note that the blue curve took less time (5min3s) to acquire, yet provided more PLD values than the gray curve (19min47s). The two curves manifest similar signal intensities and temporal characteristics. Scatter plots of E and PS obtained from the two methods are shown in Figure 7b, suggesting a good agreement between them (correlation-coefficient E: 0.87; PS: 0.92). Average E calculated from the multiple single-PLD sequence and the LL sequence was 96.4±0.6% and 97.0±0.7%, respectively. The average PS was 198.0±7.2mL/100g/min and 214.2.6±13.9mL/100g/min, respectively. Paired t-test did not show a significant difference ($P>0.05$ for both E and PS).

Study IV – Enhancing sensitivity by CO$_2$ inhalation

Hypercapnia challenge induced an increase of end-tidal CO_2 from 39.8±1.4mmHg in room air to 43.2±1.5mmHg under 2.5% CO_2 and 42.4±1.3mmHg under 2.5% CO_2 and 58% O_2 (N=5). No discomfort was reported from any of the participants. Averaged SSS signal curves under three gas conditions are shown in Figure 8a. Their coefficients-of-variation (CoV), defined as the standard deviation of the signal at optimal PLD divided by the mean, are shown in Figure

8b. Compared to the normocapnia curve, the hypercapnia curve showed a considerable increase in signal intensity (by 142±51%). CoV was reduced (P=0.028), thus SNR (as 1/CoV) increased significantly (by 78±25%, P=0.025) (Figure 8b), suggesting that hypercapnia has a considerable benefit in enhancing the sensitivity of the WEPCAST technique. Hyperoxic-hypercapnia, on the other hand, did not further increase the signal (Figure 8a and b), despite the expected increase in blood T_2^*. We attributed this to the reason that arterial blood T_1 will decrease under hyperoxic conditions, resulting in a faster decay of the labeling effects.

Figure 9 summarizes physiological parameters measured under normocapnia and hypercapnia conditions. We found that CBF increased during hypercapnia (normocapnia: 56.2±3.2mL/100g/min; hypercapnia: 66.0±4.2mL/100g/min; 17.4% change, p=0.026, one-tail t test). BAT to the SSS decreases during hypercapnia (normocapnia: 4.81±0.33s; hypercapnia: 4.31±0.15s; 10.4% change, p=0.158, one-tail t test). The fraction of venous spins, $1 - E$, also showed an increase in response to CO_2 (normocapnia: 2.0±0.7%; hypercapnia: 3.5±1.0%; 80% change, p=0.159, one-tail t test). The *PS* values, on the other hand, remained at a similar level (normocapnia: 240.9±21.5mL/100g/min; hypercapnia: 231.9±13.1mL/100g/min; 3.7% change, p=0.375, one-tail t test), because the effects of *E* and CBF offset each other in the calculation of *PS*. Note, however, that the standard error of the estimation is considerably smaller in the hypercapnia data, presumably due to enhancing signal reliability.

DISCUSSION

In this study, we proposed a non-contrast method for the measurement of BBB permeability to water by detecting ASL labeled spins in draining veins, specifically in the superior sagittal sinus. Our results suggested that arterial spins that are not exchanged to the tissue space and remain in the vessel can be detected with advanced sequence considerations. We further showed that the amount of venous ASL spins can be used to estimate physiological properties of the BBB, specifically the water extraction fraction, *E*, and permeability, *PS*. We compared pulse sequences and physiological conditions for these measurements.

Clinically, there are no existing techniques to non-invasively measure water permeability of BBB. However, several invasive methods have been developed in the literature. One is through the intracarotid injection of radiolabeled water, followed by the measurement of the extraction of the radiotracer by sampling the cerebral venous blood or external detection of

residual time course with scintillation detector (25,26,28). Another technique is based on positron emission tomography (PET) and uses intravenous injection of [^{15}O] water and [^{11}C] butanol, by assuming that butanol is freely diffusible across BBB (27,48). There are also emerging methods using contrast-agent based MRI. By measuring T$_1$ relaxivity after contrast agent injection, post-contrast MRI signal were found to be related to water permeability of BBB, in the absence of Gd-DTPA leakage (12,49-51). This signal, when combined with an arterial input function, was used to estimate the exchange rate. However, due to procedural or model complexities, these methods have not been widely used in clinical applications.

A few previous studies have considered the limited water exchange in the context of ASL (21-23,52,53). Some reports have applied a two-compartment exchange model to the conventional ASL signal at multiple PLDs, from which an exchange rate constant, k, was obtained (18,54,55). However, this method relies on the T$_1$ relaxation difference before and after the exchange of water molecules, thus the intrinsic signal-to-noise ratio (SNR) of this method is limited (56). Other studies aimed to separate blood and tissue ASL spins based on their T$_2$ relaxation time (23,57-59). However, the T$_2$ difference can also be due to oxygenation changes as the spin flows from artery to capillary, to veins. A more advanced technique is to use diffusion or intra-vascular-incoherent-motion (IVIM) weighted ASL to separate microvascular and extravascular signals by applying magnetic field gradients (60-62), which can then give water exchange rate between the two compartments by fitting the signal to a tracer kinetic model (19,20,63). A confounding factor of this method is that it relies on the assumption that diffusion gradients can fully remove vascular signal while having no effect on the tissue signal. The present technique separates the vessel spins from those in the tissue by a combination of spatial location (i.e. in the SSS) and flow velocity (i.e. phase-contrast velocity-encoding), thus may provide a more reliable assessment.

The average *E* value we measured was 96.2±0.6% and that for *PS* was 199.9±8.3mL/100g/min. *PS* values reported in previous literature were: 169mL/100g/min in human with outflow sampling method (28), 138mL/100g/min in rhesus monkey with residue detection technique (25), 104mL/100g/min and 133mL/100g/min in human with dual label PET method (27,48), between 240 to 453mL/100g/min in human with contrast-based MRI (49,50), 204mL/100g/min in human with T$_2$-ASL (57), and 208mL/100g/min in human with DW-ASL (20). Our results overall showed good agreement with previous literature. The PET literature

showed generally lower *PS* values. This was previously attributed to the notion that the inclusion of metabolically inactive CSF spaces and partial voluming effect of a nearby sulcus would cause an underestimation of *PS* (27).

In this study, we proposed a new sequence, WEPCAST MRI, by using phase-contrast velocity-encoding to selectively highlight the vascular signal in ASL data. This was found to be critical in minimizing tissue perfusion confounds in our signal curve. When similarly applying the velocity-encoding in the M_0 images, the partial volume effects (from tissue) in our data can be completely accounted for, despite using a thick imaging slice. Although beyond the scope of this study, we point out that the WEPCAST sequence may also be useful in dynamic ASL angiography (64-66) that aims to measure arterial ASL signal only.

Another technical emphasis of this study was on the background suppression of unwanted signals. Background suppression has been widely used in single-PLD ASL to reduce physiologic noise (37,67). A requirement specific for this technique is that the control blood signal needs to be sufficiently suppressed (which is not an issue in conventional ASL because blood signal is <5% of the voxel). We have therefore added blood-suppressing pulses to the sequence as well. The benefit of these considerations can be seen from the results of Study III, which showed that robust SSS ASL signal was only obtained when both static tissue signal and blood vessel control signal are sufficiently attenuated.

In this study, we also demonstrated the benefit of hypercapnia on the sensitivity of our technique. Consistent with known physiology (45,68), hypercapnia results in an increase of CBF by around 17% and a decrease of BAT by around 10%. Collectively, these effects resulted in an almost doubling of the WEPCAST MRI signal intensity (Figure 8). It is important to note that, while *E* reduced from 98% to 96% (due to the increase in CBF), the measure of permeability, *PS*, remained at a similar level. This is consistent with findings of Eichling et al (25) and Raichle et al (26) that *E* decreases with flow alteration induced by change in $PaCO_2$ while *PS* was unaltered by hypocapnia or hypercapnia. However, it remains to be determined whether hypercapnia will alter *PS* in patients with neurological diseases, which should be the subject of future investigations.

One limitation of our study is that we only measured the global permeability of BBB, without spatial information. While many diseases, e.g. Alzheimer's disease, multiple sclerosis, ALS, stroke and lysosomal storage disease, affect a large portion of the brain and therefore may

benefit from this technique, it is expected that its sensitivity to focal brain diseases may be limited. Further improvements of imaging techniques are needed to provide region-specific BBB information. Another limitation is that, at baseline, most (~95%) of the ASL spins are already extracted to the tissue, leaving limited spins to be measured in the veins. For a disease that causes BBB to be more permeable, even fewer ASL spins will be present in the SSS thus the ability to reliably detect the signal may be further compromised. This can be alleviated by a CBF-enhancing maneuver such as CO_2 inhalation that was demonstrated in the present study. Additionally, the proposed method will have the same limitations as conventional ASL methods, including that the SNR may be low when the flow is slow and the signal quantification is dependent on several assumptions such as inversion efficiency and blood/tissue T_1 values. Higher field could be potentially beneficial due to longer blood T_1 and larger intrinsic SNR, although B0 and B1 inhomogeneity at higher field may negatively impact the signal.

CONCLUSION

In this study, we proposed a non-contrast MRI technique for the assessment of global BBB permeability by detecting ASL signal in venous vessels. We developed a pulse sequence, WEPCAST MRI, that is specifically optimized for this purpose. The estimated permeability index was in good agreement with prior literature using invasive methods. We also demonstrated that a mild hypercapnia using 2.5% CO_2 can significantly enhance the sensitivity of this technique without causing discomfort.

17

REFERENCES

1. Abbott NJ, Patabendige AA, Dolman DE, Yusof SR, Begley DJ. Structure and function of the blood-brain barrier. Neurobiol Dis 2010;37:13-25.
2. Bell RD, Zlokovic BV. Neurovascular mechanisms and blood-brain barrier disorder in Alzheimer's disease. Acta Neuropathol 2009;118:103-113.
3. Kermode AG, Thompson AJ, Tofts P, MacManus DG, Kendall BE, Kingsley DP, Moseley IF, Rudge P, McDonald WI. Breakdown of the blood-brain barrier precedes symptoms and other MRI signs of new lesions in multiple sclerosis. Pathogenetic and clinical implications. Brain 1990;113 (Pt 5):1477-1489.
4. Zlokovic BV. The blood-brain barrier in health and chronic neurodegenerative disorders. Neuron 2008;57:178-201.
5. Long DM. Capillary ultrastructure and the blood-brain barrier in human malignant brain tumors. J Neurosurg 1970;32:127-144.
6. Sandoval KE, Witt KA. Blood-brain barrier tight junction permeability and ischemic stroke. Neurobiol Dis 2008;32:200-219.
7. Desai BS, Monahan AJ, Carvey PM, Hendey B. Blood-brain barrier pathology in Alzheimer's and Parkinson's disease: implications for drug therapy. Cell Transplant 2007;16:285-299.
8. Kroll RA, Neuwelt EA. Outwitting the blood-brain barrier for therapeutic purposes: osmotic opening and other means. Neurosurgery 1998;42:1083-1099; discussion 1099-1100.
9. Doolittle ND, Miner ME, Hall WA et al. Safety and efficacy of a multicenter study using intraarterial chemotherapy in conjunction with osmotic opening of the blood-brain barrier for the treatment of patients with malignant brain tumors. Cancer 2000;88:637-647.
10. Gabathuler R. Approaches to transport therapeutic drugs across the blood-brain barrier to treat brain diseases. Neurobiol Dis 2010;37:48-57.
11. Tofts PS, Kermode AG. Measurement of the blood-brain barrier permeability and leakage space using dynamic MR imaging. 1. Fundamental concepts. Magn Reson Med 1991;17:357-367.
12. Barbier EL, St Lawrence KS, Grillon E, Koretsky AP, Decorps M. A model of blood-brain barrier permeability to water: accounting for blood inflow and longitudinal relaxation effects. Magn Reson Med 2002;47:1100-1109.
13. Starr JM, Farrall AJ, Armitage P, McGurn B, Wardlaw J. Blood-brain barrier permeability in Alzheimer's disease: a case-control MRI study. Psychiatry Res 2009;171:232-241.
14. van de Haar HJ, Burgmans S, Jansen JF, van Osch MJ, van Buchem MA, Muller M, Hofman PA, Verhey FR, Backes WH. Blood-Brain Barrier Leakage in Patients with Early Alzheimer Disease. Radiology 2016;281:527-535.
15. Olchowy C, Cebulski K, Lasecki M, Chaber R, Olchowy A, Kalwak K, Zaleska-Dorobisz U. The presence of the gadolinium-based contrast agent depositions in the brain and symptoms of gadolinium neurotoxicity - A systematic review. PLoS One 2017;12:e0171704.
16. Kanda T, Oba H, Toyoda K, Furui S. Recent Advances in Understanding Gadolinium Retention in the Brain. AJNR Am J Neuroradiol 2016;37:E1-2.
17. Cornford EM, Hyman S. Blood-brain barrier permeability to small and large molecules. Adv Drug Deliv Rev 1999;36:145-163.
18. Parkes LM, Tofts PS. Improved accuracy of human cerebral blood perfusion measurements using arterial spin labeling: accounting for capillary water permeability. Magn Reson Med 2002;48:27-41.
19. Wang J, Fernandez-Seara MA, Wang S, St Lawrence KS. When perfusion meets diffusion: in vivo measurement of water permeability in human brain. J Cereb Blood Flow Metab 2007;27:839-849.

20. St Lawrence KS, Owen D, Wang DJ. A two-stage approach for measuring vascular water exchange and arterial transit time by diffusion-weighted perfusion MRI. Magn Reson Med 2012;67:1275-1284.
21. Zhou J, Wilson DA, Ulatowski JA, Traystman RJ, van Zijl PC. Two-compartment exchange model for perfusion quantification using arterial spin tagging. J Cereb Blood Flow Metab 2001;21:440-455.
22. St Lawrence KS, Frank JA, McLaughlin AC. Effect of restricted water exchange on cerebral blood flow values calculated with arterial spin tagging: a theoretical investigation. Magn Reson Med 2000;44:440-449.
23. Liu P, Uh J, Lu H. Determination of spin compartment in arterial spin labeling MRI. Magn Reson Med 2011;65:120-127.
24. Fernandez-Seara MA, Wang Z, Wang J, Rao HY, Guenther M, Feinberg DA, Detre JA. Continuous arterial spin labeling perfusion measurements using single shot 3D GRASE at 3 T. Magn Reson Med 2005;54:1241-1247.
25. Eichling JO, Raichle ME, Grubb RL, Jr., Ter-Pogossian MM. Evidence of the limitations of water as a freely diffusible tracer in brain of the rhesus monkey. Circ Res 1974;35:358-364.
26. Raichle ME, Eichling JO, Straatmann MG, Welch MJ, Larson KB, Ter-Pogossian MM. Blood-brain barrier permeability of 11C-labeled alcohols and 15O-labeled water. Am J Physiol 1976;230:543-552.
27. Herscovitch P, Raichle ME, Kilbourn MR, Welch MJ. Positron emission tomographic measurement of cerebral blood flow and permeability-surface area product of water using [15O]water and [11C]butanol. J Cereb Blood Flow Metab 1987;7:527-542.
28. Paulson OB, Hertz MM, Bolwig TG, Lassen NA. Filtration and diffusion of water across the blood-brain barrier in man. Microvasc Res 1977;13:113-124.
29. Renkin EM. Transport of potassium-42 from blood to tissue in isolated mammalian skeletal muscles. Am J Physiol 1959;197:1205-1210.
30. Crone C. The Permeability of Capillaries in Various Organs as Determined by Use of the 'Indicator Diffusion' Method. Acta Physiol Scand 1963;58:292-305.
31. Alsop DC, Detre JA, Golay X et al. Recommended implementation of arterial spin-labeled perfusion MRI for clinical applications: A consensus of the ISMRM perfusion study group and the European consortium for ASL in dementia. Magn Reson Med 2015;73:102-116.
32. Detre JA, Alsop DC. Perfusion magnetic resonance imaging with continuous arterial spin labeling: methods and clinical applications in the central nervous system. Eur J Radiol 1999;30:115-124.
33. Gonzalez-At JB, Alsop DC, Detre JA. Cerebral perfusion and arterial transit time changes during task activation determined with continuous arterial spin labeling. Magn Reson Med 2000;43:739-746.
34. Peng SL, Dumas JA, Park DC, Liu P, Filbey FM, McAdams CJ, Pinkham AE, Adinoff B, Zhang R, Lu H. Age-related increase of resting metabolic rate in the human brain. Neuroimage 2014;98:176-183.
35. Li W, Liu P, Lu H, Strouse JJ, van Zijl PCM, Qin Q. Fast measurement of blood T1 in the human carotid artery at 3T: Accuracy, precision, and reproducibility. Magn Reson Med 2017;77:2296-2302.
36. Aslan S, Xu F, Wang PL, Uh J, Yezhuvath US, van Osch M, Lu H. Estimation of labeling efficiency in pseudocontinuous arterial spin labeling. Magn Reson Med 2010;63:765-771.
37. Robson PM, Madhuranthakam AJ, Dai W, Pedrosa I, Rofsky NM, Alsop DC. Strategies for reducing respiratory motion artifacts in renal perfusion imaging with arterial spin labeling. Magn Reson Med 2009;61:1374-1387.
38. Krishnamurthy LC, Liu P, Ge Y, Lu H. Vessel-specific quantification of blood oxygenation with T2-relaxation-under-phase-contrast MRI. Magn Reson Med 2014;71:978-989.

39.   Schuchardt F, Schroeder L, Anastasopoulos C, Markl M, Bauerle J, Hennemuth A, Drexl J, Valdueza JM, Mader I, Harloff A. In vivo analysis of physiological 3D blood flow of cerebral veins. Eur Radiol 2015;25:2371-2380.
40.   Gunther M, Bock M, Schad LR. Arterial spin labeling in combination with a look-locker sampling strategy: inflow turbo-sampling EPI-FAIR (ITS-FAIR). Magn Reson Med 2001;46:974-984.
41.   Hendrikse J, Lu H, van der Grond J, Van Zijl PC, Golay X. Measurements of cerebral perfusion and arterial hemodynamics during visual stimulation using TURBO-TILT. Magn Reson Med 2003;50:429-433.
42.   Petersen ET, Lim T, Golay X. Model-free arterial spin labeling quantification approach for perfusion MRI. Magn Reson Med 2006;55:219-232.
43.   Petersen ET, Mouridsen K, Golay X, all named co-authors of the Qt-rs. The QUASAR reproducibility study, Part II: Results from a multi-center Arterial Spin Labeling test-retest study. Neuroimage 2010;49:104-113.
44.   Lu H, Liu P, Yezhuvath U, Cheng Y, Marshall O, Ge Y. MRI mapping of cerebrovascular reactivity via gas inhalation challenges. J Vis Exp 2014. doi: 10.3791/52306.
45.   Donahue MJ, Faraco CC, Strother MK, Chappell MA, Rane S, Dethrage LM, Hendrikse J, Siero JC. Bolus arrival time and cerebral blood flow responses to hypercarbia. J Cereb Blood Flow Metab 2014;34:1243-1252.
46.   Yezhuvath US, Lewis-Amezcua K, Varghese R, Xiao G, Lu H. On the assessment of cerebrovascular reactivity using hypercapnia BOLD MRI. NMR Biomed 2009;22:779-786.
47.   Garcia DM, Duhamel G, Alsop DC. Efficiency of inversion pulses for background suppressed arterial spin labeling. Magn Reson Med 2005;54:366-372.
48.   Berridge MS, Adler LP, Nelson AD, Cassidy EH, Muzic RF, Bednarczyk EM, Miraldi F. Measurement of human cerebral blood flow with [15O]butanol and positron emission tomography. J Cereb Blood Flow Metab 1991;11:707-715.
49.   Schwarzbauer C, Morrissey SP, Deichmann R, Hillenbrand C, Syha J, Adolf H, Noth U, Haase A. Quantitative magnetic resonance imaging of capillary water permeability and regional blood volume with an intravascular MR contrast agent. Magn Reson Med 1997;37:769-777.
50.   Rooney WD, Li X, Sammi MK, Bourdette DN, Neuwelt EA, Springer CS, Jr. Mapping human brain capillary water lifetime: high-resolution metabolic neuroimaging. NMR Biomed 2015;28:607-623.
51.   Uh J, Yezhuvath U, Cheng Y, Lu H. In vivo vascular hallmarks of diffuse leukoaraiosis. J Magn Reson Imaging 2010;32:184-190.
52.   St Lawrence KS, Wang J. Effects of the apparent transverse relaxation time on cerebral blood flow measurements obtained by arterial spin labeling. Magn Reson Med 2005;53:425-433.
53.   Ewing JR, Cao Y, Fenstermacher J. Single-coil arterial spin-tagging for estimating cerebral blood flow as viewed from the capillary: relative contributions of intra- and extravascular signal. Magn Reson Med 2001;46:465-475.
54.   Li KL, Zhu X, Hylton N, Jahng GH, Weiner MW, Schuff N. Four-phase single-capillary stepwise model for kinetics in arterial spin labeling MRI. Magn Reson Med 2005;53:511-518.
55.   Hales PW, Clark CA. Combined arterial spin labeling and diffusion-weighted imaging for noninvasive estimation of capillary volume fraction and permeability-surface product in the human brain. J Cereb Blood Flow Metab 2013;33:67-75.
56.   Carr JP, Buckley DL, Tessier J, Parker GJ. What levels of precision are achievable for quantification of perfusion and capillary permeability surface area product using ASL? Magn Reson Med 2007;58:281-289.
57.   Gregori J, Schuff N, Kern R, Gunther M. T2-based arterial spin labeling measurements of blood to tissue water transfer in human brain. J Magn Reson Imaging 2013;37:332-342.

58.   Wells JA, Siow B, Lythgoe MF, Thomas DL. Measuring biexponential transverse relaxation of the ASL signal at 9.4 T to estimate arterial oxygen saturation and the time of exchange of labeled blood water into cortical brain tissue. J Cereb Blood Flow Metab 2013;33:215-224.

59.   Ohene Y, Harrison IF, Nahavandi P, Ismail O, Thomas DL, Lythgoe MF, Wells JA. Non-invasive Assessment of Vascular Water Permeability in the Mouse Brain using multi-TE ASL. Proceedings of the 25th Annual Meeting of ISMRM, Honolulu, HI, USA, 2017. p 0475.

60.   Zhang X, Ingo C, Teeuwisse WM, Chen Z, van Osch MJP. Comparison of perfusion signal acquired by arterial spin labeling-prepared intravoxel incoherent motion (IVIM) MRI and conventional IVIM MRI to unravel the origin of the IVIM signal. Magn Reson Med 2017. doi: 10.1002/mrm.26723.

61.   Kim T, Kim SG. Quantification of cerebral arterial blood volume using arterial spin labeling with intravoxel incoherent motion-sensitive gradients. Magn Reson Med 2006;55:1047-1057.

62.   Wells JA, Thomas DL, Saga T, Kershaw J, Aoki I. MRI of cerebral micro-vascular flow patterns: A multi-direction diffusion-weighted ASL approach. J Cereb Blood Flow Metab 2017;37:2076-2083.

63.   Tiwari YV, Lu J, Shen Q, Cerqueira B, Duong TQ. Magnetic resonance imaging of blood-brain barrier permeability in ischemic stroke using diffusion-weighted arterial spin labeling in rats. J Cereb Blood Flow Metab 2017;37:2706-2715.

64.   Okell TW, Chappell MA, Woolrich MW, Gunther M, Feinberg DA, Jezzard P. Vessel-encoded dynamic magnetic resonance angiography using arterial spin labeling. Magn Reson Med 2010;64:430-438.

65.   Sallustio F, Kern R, Gunther M, Szabo K, Griebe M, Meairs S, Hennerici M, Gass A. Assessment of intracranial collateral flow by using dynamic arterial spin labeling MRA and transcranial color-coded duplex ultrasound. Stroke 2008;39:1894-1897.

66.   van Osch MJ, Hendrikse J, Golay X, Bakker CJ, van der Grond J. Non-invasive visualization of collateral blood flow patterns of the circle of Willis by dynamic MR angiography. Med Image Anal 2006;10:59-70.

67.   Vidorreta M, Wang Z, Rodriguez I, Pastor MA, Detre JA, Fernandez-Seara MA. Comparison of 2D and 3D single-shot ASL perfusion fMRI sequences. Neuroimage 2013;66:662-671.

68.   Su P, Mao D, Liu P, Li Y, Pinho MC, Welch BG, Lu H. Multiparametric estimation of brain hemodynamics with MR fingerprinting ASL. Magn Reson Med 2016. doi: 10.1002/mrm.26587.
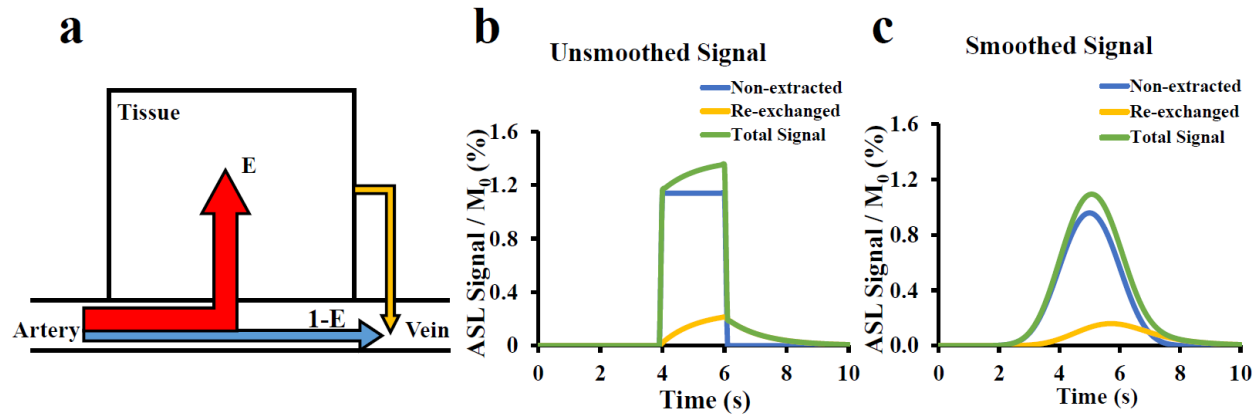
Figures

Figure 1: Concept and simulations of the proposed method. (a) Illustration of the conceptual model used to describe water extraction around BBB in capillary. Most of incoming labeled spins are extracted by tissue (red arrow) while a small fraction is drained to the vein (blue). Additionally, some of the labeled spins that were extracted to tissue are re-exchanged back to the vein (yellow arrow). (b) Simulation results of ASL signal at SSS without considering dispersion (unsmoothed). Non-extracted spins contributed most of the signal compared with re-exchanged spins. Simulation parameters: $T_{1,blood}$=1841ms (35), $T_{1,tissue}$=1165ms (23), α=0.86 (36), E=0.95 (28), δ_v=4s (23) and λ=0.9mL/g (31). (c) Simulation results of ASL signal after Gaussian smoothing, which accounts for effects of bolus dispersion and variations in bolus arrival time.
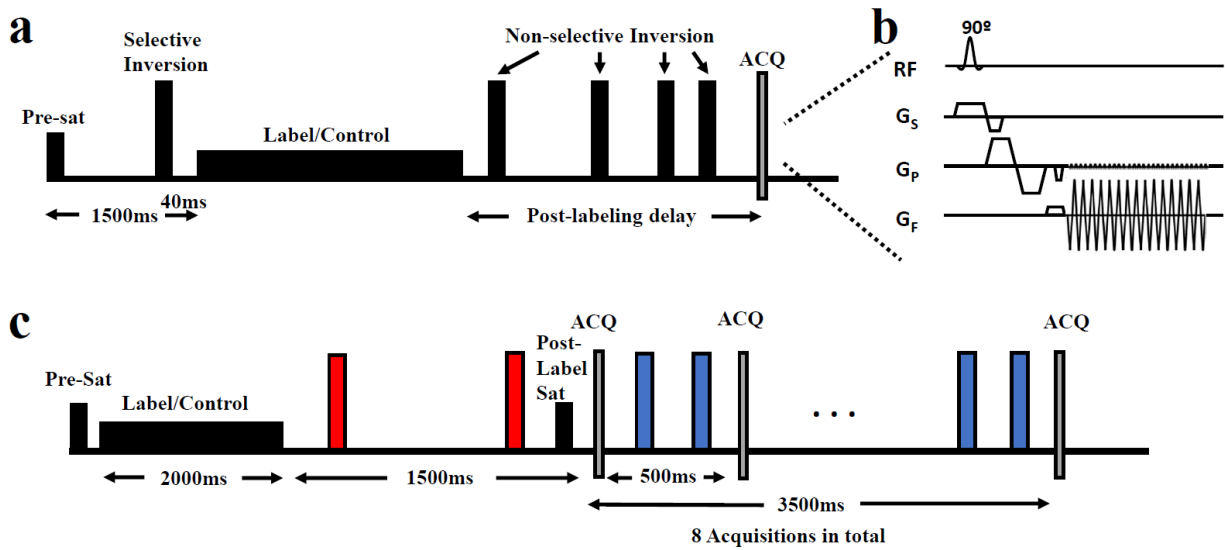
Figure 2: Schematics of pulse sequences used in this study. (a) A conventional ASL sequence with a five-inversion background-suppression. (b) WEPCAST MRI sequence with flow-sensitive bipolar gradient added in the acquisition module. (c) Look-Locker WEPCAST MRI with background-suppression at all PLDs. The red pulses are vessel suppression pulses while the blue ones are tissue suppression pulses.
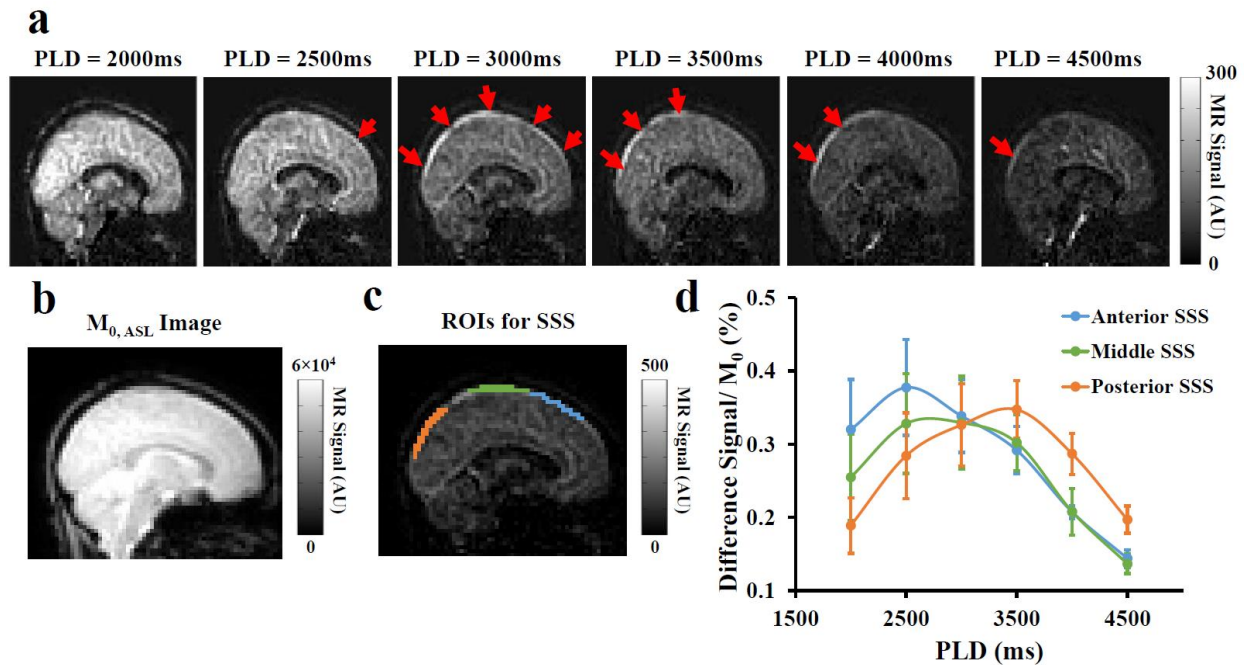
Figure 3: Venous ASL signals using conventional pCASL with long PLDs. (a) Representative difference images using conventional ASL with very long PLDs. ASL signal became visible in SSS starting from PLD=2500 ms (red arrows), reached a peak at around PLD=3000-3500ms, and then decayed afterwards. (b) $M_{0,ASL}$ image. (c) ROIs corresponding to anterior, middle and posterior SSS that were used for quantitative analysis. (d) Group-averaged ROI signals from anterior, middle and posterior segments of the SSS. The signal curve shifts toward the right as the ROI moves from anterior to posterior region. Error bar denotes the standard error across participants (N=6).
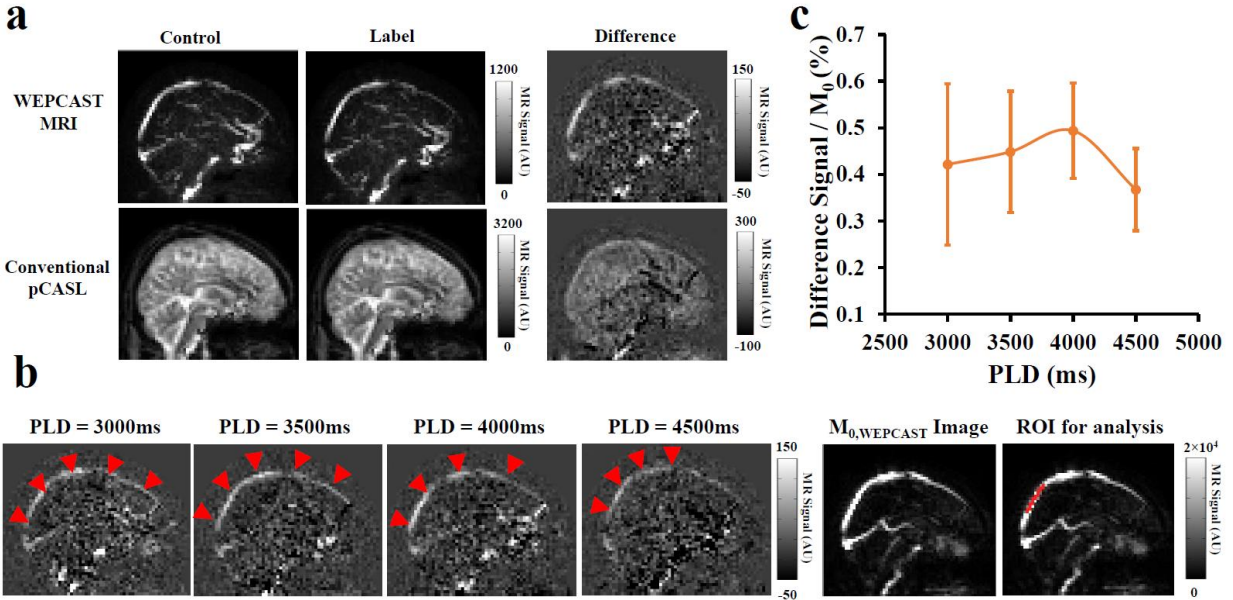
Figure 4: Venous ASL signal measured with WEPCAST MRI. (a) Representative images using the WEPCAST sequence (at PLD of 4000ms). Due to the flow-encoding, the control and label images show only large vessels without partial voluming of tissue signal. The vessel contour in the difference image is very clear. Conventional pCASL images are also shown, in which the vessel is not apparent in the difference image. (b) WEPCAST difference images as a function of PLD, as well as the M_0 image that is used to normalize the difference images. Also shown is an illustration of ROI used for quantitative analysis. (c) Group-averaged ROI results of posterior SSS signal. Error bar denotes the standard error across participants (N=6). Note that different participants have peak signals at different PLDs, resulting in a relatively large error bar.
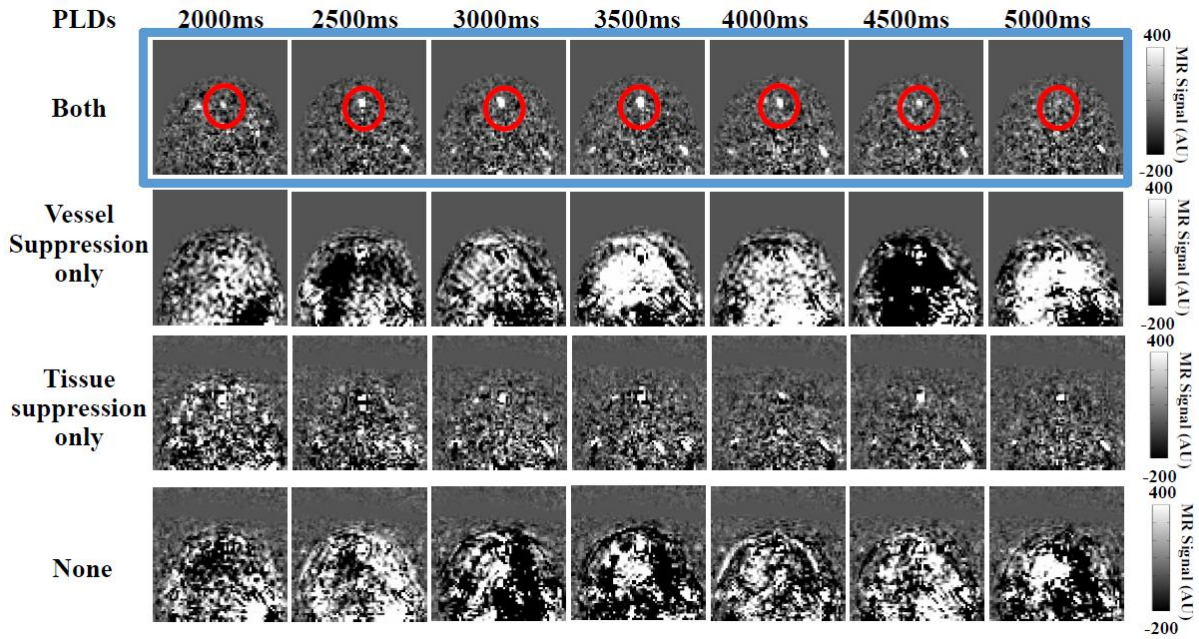
Figure 5: Look-Locker WEPCAST results. Representative difference images using four sequences with different background-suppression schemes. Only the sequence with both tissue and vessel suppression pulses (blue box) shows conspicuous venous ASL signal (red circles) throughout the PLD values.
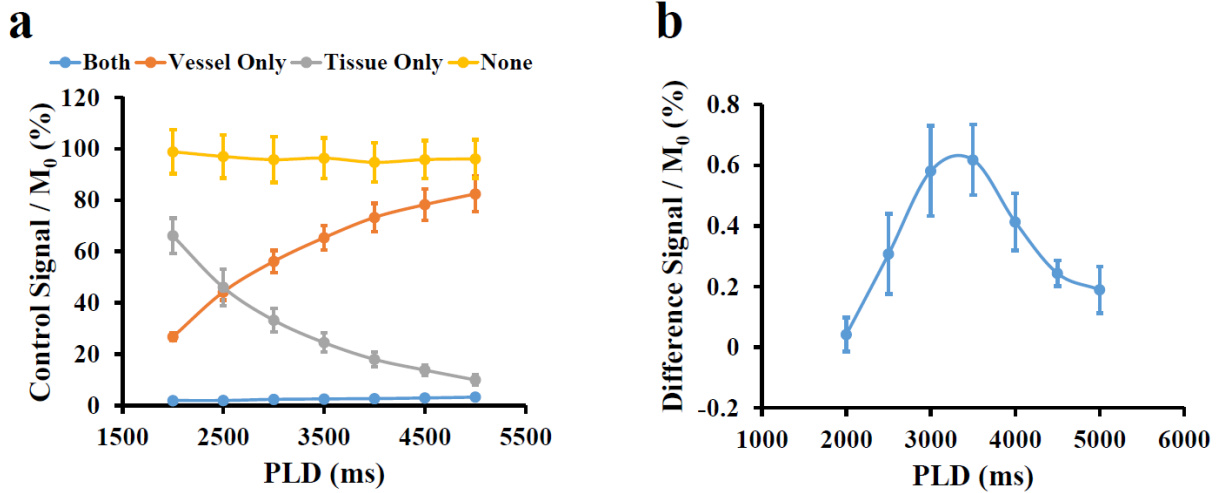
Figure 6: Quantitative results of Look-Locker WEPCAST MRI. (a) Control signal in SSS using the four sequences with different background suppression schemes (averaged over 6 subjects). Only the sequence with both suppression pulses can suppress the signal to less than 5% of M_0. (b) Difference signal in the "vessel-and-tissue suppression" scan as a function of PLD. Error bar denotes the standard error across participants.
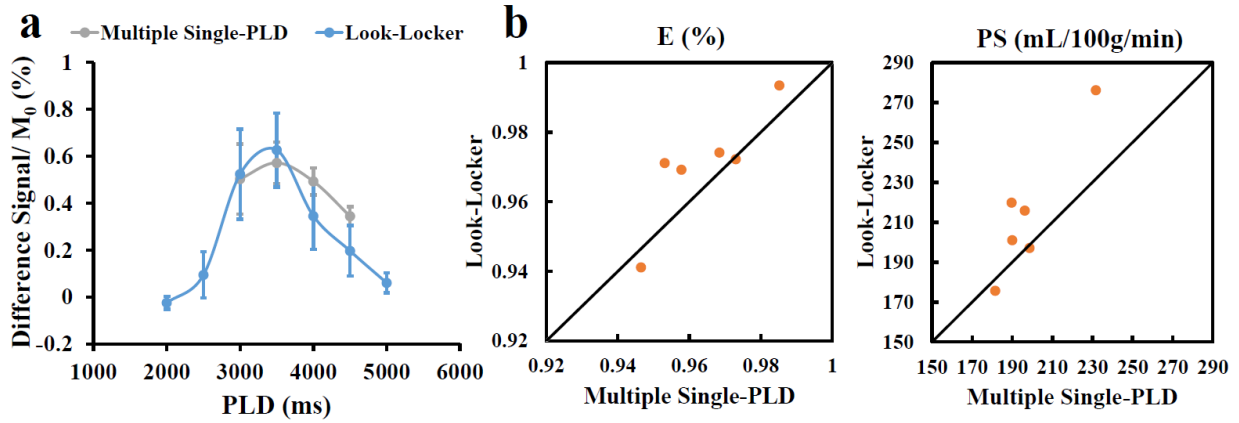
Figure 7: Comparison of LL-WEPCAST with single-PLD WEPCAST. (a) Averaged signal curves (N=6) obtained from multiple single-PLD WEPCAST and LL-WEPCAST. Error bar denotes the standard error across participants. (b) Scatter plots of *E* and *PS* measured with the two methods. Each symbol represents data from one subject.
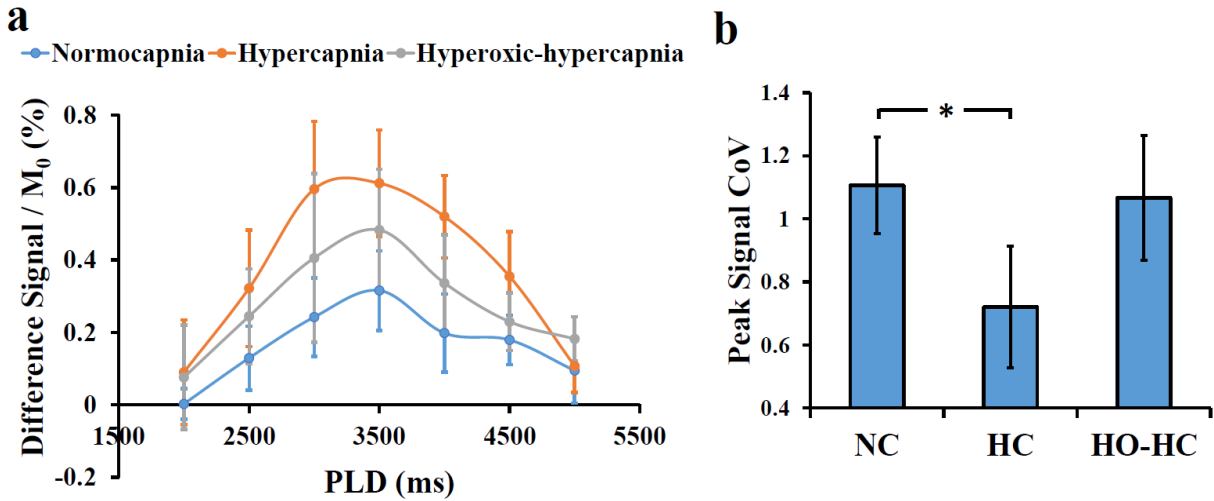
Figure 8: LL-WEPCAST MRI signal with physiological challenges (a) Averaged signal curve from SSS ROI (N=5) under normocapnia, hypercapnia (2.5% CO_2), and hyperoxic-hypercapnia (2.5%CO_2 and 58% O_2). Hypercapnia dramatically increased the signal while hyperoxic-hypercapnia only showed a modest benefit. Error bar denotes the standard error across participants. (b) Coefficient-of-variation (CoV) of peak signal under three physiological conditions. Lower CoV indicates better SNR. NC: normocapnia. HC: hypercapnia. HO-HC: hyperoxic-hypercapnia.
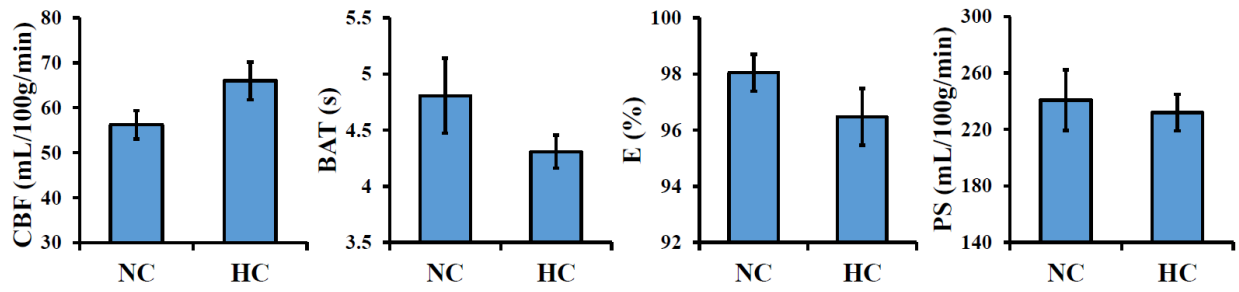
Figure 9: Physiological parameters estimated under different conditions. Error bars denote standard error across subjects.

Table 1: Dependence of estimated parameters on model assumptions. The experimental data were analyzed several times, each using slightly different ($\pm10\%$) assumed values for $T_{1,blood}$, $T_{1,tissue}$, and α.

Estimated parameter	Original	$T_{1,blood}$ -10%	$T_{1,blood}$ +10%	$T_{1,tissue}$ -10%	$T_{1,tissue}$ +10%	α -10%	α +10%
E (%)	95.5%	93.9%	96.6%	95.3%	95.6%	94.8%	96.0%
PS (mL/100g/min)	188.9	182.5	204.7	187.6	193.4	182.5	198.0

Supporting Information

Supporting Methods

        The blood spins in superior sagittal sinus (SSS) consist of following three components: (a) non-extracted arterial spins; (b) extracted arterial spins that were re-exchanged into vessel; and (c) non-labeled spins that came to vessel from tissue through exchange.

        For part (a), i.e. non-extracted arterial spins, the signal under control condition can be written as

$$M_{a,ctrl}(t) = (1 - E)M_{0,blood}c(t), \tag{S1}$$

where E is the extraction fraction of water and $M_{0,blood}$ is the equilibrium magnetization of blood (MR signal/100 mL blood), $c(t) = \begin{cases} 1, & if\, \delta_v < t < \delta_v + \tau \\ 0, & otherwise \end{cases}$ is the arterial input function, δ_v is bolus arrival time (BAT) of spins to SSS, and τ is labeling duration. The signal under label condition can be written as

$$M_{a,labl}(t) = (1 - E)M_{0,blood}(1 - 2\alpha e^{-\frac{\delta_v}{T_{1,blood}}})c(t), \tag{S2}$$

where $T_{1,blood}$ is blood T$_1$ and α is the labeling efficiency. The ASL difference signal from part (a) is then

$$\Delta M_a(t) = 2\alpha(1 - E)M_{0,blood}e^{-\frac{\delta_v}{T_{1,blood}}}c(t), \tag{S3}$$

which is used as Eq. [2] in the main text.

        For part (b), to calculate signal in veins at time t, let us first consider signal in the tissue at time $t - \delta_{tv}$, in which δ_{tv} denoted the time it takes for the blood to travel from tissue to vein. This is useful because once tissue signal at time $t - \delta_{tv}$ is calculated, the venous signal at time t simply follows longitudinal relaxation at $T_{1,blood}$ for a period of δ_{tv}. Based on ASL kinetic model (1), label signal in tissue at $t - \delta_{tv}$ can be written as:

$$M_{tissue,labl}(t - \delta_{tv}) = fEM_{0,blood}\int_{\delta_t}^{t-\delta_{tv}} r(t - \delta_{tv} - t')(1 -$$

$$2e^{-\frac{\delta_t}{T_{1,blood}}}m(t - \delta_{tv} - t'))dt', \tag{S4}$$

where f is cerebral blood flow (CBF), δ_t is BAT of tissue, $r(t) = e^{-ft/\lambda}$ is residue function of labeled spins in tissue, λ is blood-brain partition coefficient of water, $m(t) = e^{-t/T_{1,tissue}}$ represents T_1 relaxation in tissue.

These spins are then re-exchanged back to the vessel and become venous spins. Note that, although the amount of labeled signals in the venous voxel is the same as that in a tissue voxel, it does not mean that all of the labeled spins in the tissue has come back to vein. The labeled spins in the venous voxel actually come from many tissue voxels, each contributing a small fraction to the venous spins. Once inside the vein, these labeled spins are subject to further longitudinal relaxation at T_1 of blood. The signal evolution can be calculated by Bloch equation using Eq. [S4] as the initial magnetization. One can derive that, at time t, the signal which is now in venous vessel becomes

$$M_{b,labl}(t) = f/\lambda E M_{0,blood} \int_0^t c(t')r(t-t')(1 - 2\alpha e^{-\frac{\delta_v}{T_{1,blood}}} m(t-t'))dt', \quad [S5]$$

Following the same framework, one can derive the control signal for part (b) to be

$$M_{b,ctrl}(t) = f/\lambda E M_{0,blood} \int_0^t c(t')r(t-t')dt', \quad [S6]$$

The difference signal from part (b) is

$$\Delta M_b(t) = M_{b,ctrl}(t) - M_{b,labl}(t)$$

$$= f/\lambda E M_{0,blood} \int_0^t c(t')r(t-t')2\alpha e^{-\frac{\delta_v}{T_{1,blood}}} m(t-t')dt' \quad [S7]$$

$$= 2\alpha f/\lambda E M_{0,blood} e^{-\frac{\delta_v}{T_{1,blood}}} c(t) \otimes [r(t)m(t)].$$

which is used as Eq. [4] in the main text.

For part (c), i.e. non-labeled spins that came to vessel from tissue through exchange, the signal under control and label condition can both be written as

$$M_{c,ctrl}(t) = M_{c,labl}(t) = f/\lambda E(1 - \int_0^t c(t')r(t-t')dt')M_{0,blood}, \quad [S8]$$

Thus, the difference signal $\Delta M_c(t) = 0$.

References

1.   Buxton RB, Frank LR, Wong EC, Siewert B, Warach S, Edelman RR. A general kinetic model for quantitative perfusion imaging with arterial spin labeling. Magn Reson Med 1998;40:383-396.
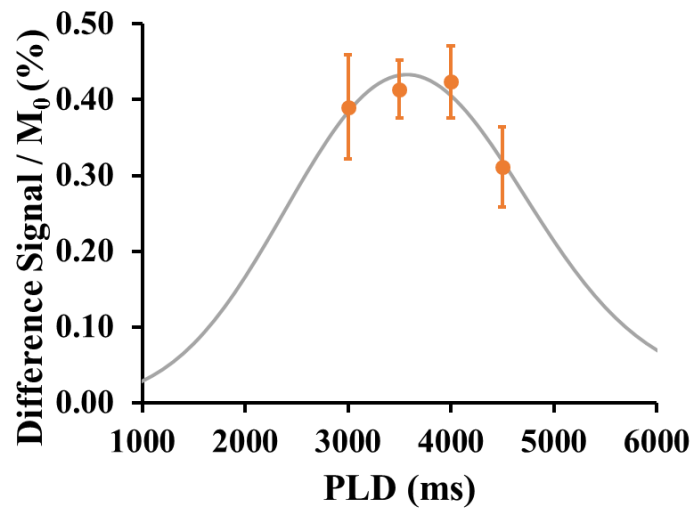
Supporting Figure S1: ROI results of posterior SSS signal for the subject shown in Figure 4 and the corresponding fitting results. Error bars denote standard errors across repetitions.
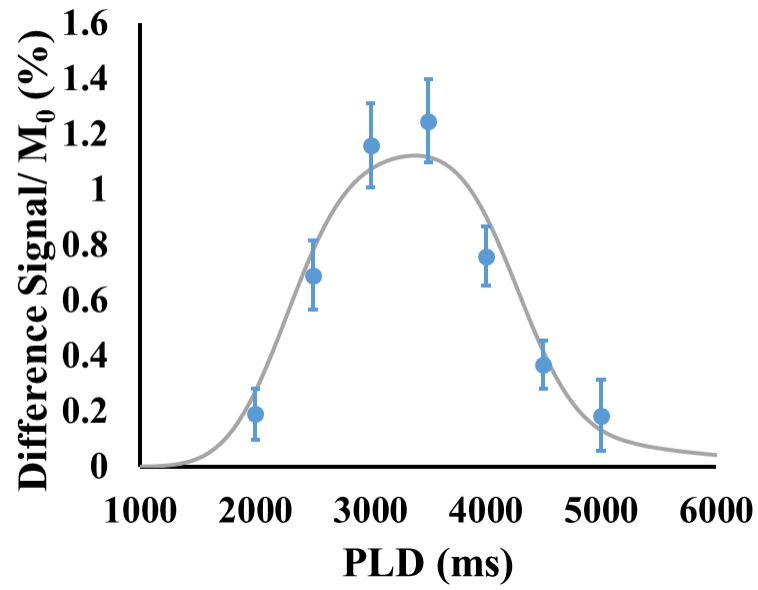
Supporting Figure S2: ROI results of posterior SSS signal for the subject shown in Figure 5 and the corresponding fitting results. Error bars denote standard errors across repetitions.
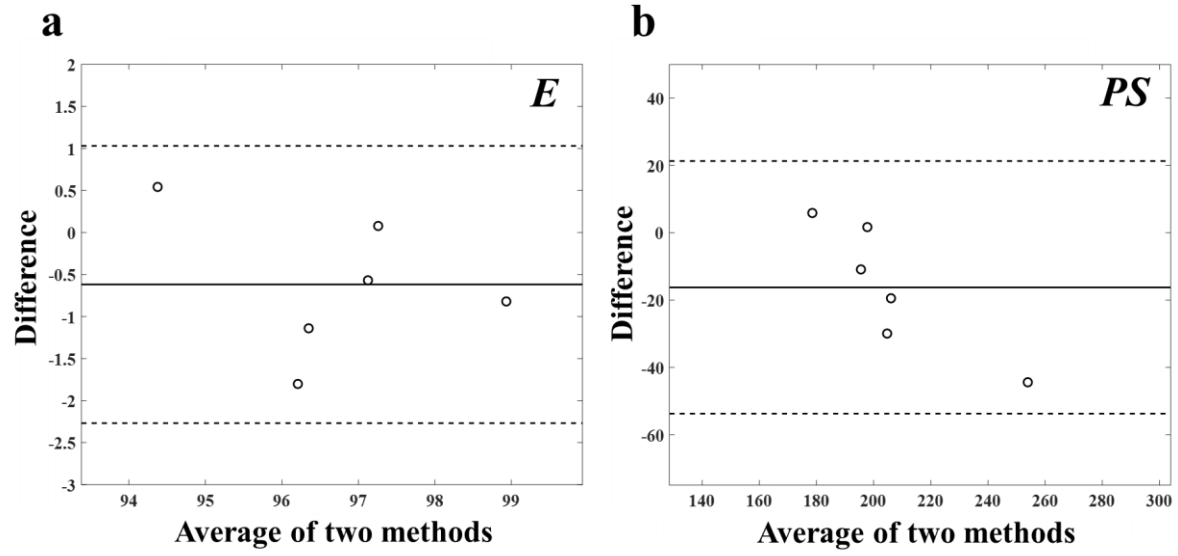
Supporting Figure S3: Bland-Altman plots for E and PS between multiple single-PLD and Look-Locker methods.